Image Transmission Utilizing Amplitude Modulation in Rydberg Atomic Antenna

Peng Zhang , Shaoxin Yuan , Mingyong Jing , Jinpeng Yuan , Hao Zhang , and Linjie Zhang

Abstract—Microwave electric field precision measurement based on Rydberg atomic quantum coherence effect has rapidly advanced in recent years, capitalizing on its high sensitivity, broad bandwidth, and traceability. The utilization of distinct Rydberg quantum states facilitates achieving an ultra-wideband measurement response across various microwave frequency bands, offering extensive applications in wireless communication, radar positioning, astronomical observation, and related domains. In this work, leveraging the Rydberg atomic antenna, we achieve simultaneous multi-frequency reception in the C-band (7.91 GHz, 5.106 GHz) and S-band (3.78 GHz) through amplitude-shift keying modulation. Furthermore, we encode RGB information from color image pixels onto 3 carrier frequencies in the C-band and S-band, while optimizing the multi-channel signal amplitude. The pixel information of the color image obtained by atomic demodulation realizes the high-fidelity digital color image transmission, with a root mean square error of 4.806, a mean square signal-to-noise ratio of 1.627, a peak signal-to-noise ratio of 29.998 and a structural similarity index of 0.9589. This study establishes an experimental groundwork for the utilization of Rydberg atomic antennas in ultra-wideband wireless communication and measurement.

Index Terms—Amplitude shift keying, frequency encoding, image transmission, Rydberg atom.

I. INTRODUCTION

THE Rydberg atom refers to an atom in a highly excited state, where the outermost electron is elevated to a significantly large principal quantum number, denoted as n [1], [2], [3]. This state resembles a hydrogen-like atomic structure consisting of an atom and an outer electron, imparting unique properties to the Rydberg atom. The polarizability of a Rydberg atom, characterized by its principal quantum number n, follows a proportional relationship with n^7. Additionally, the electric field strength threshold for field ionization is inversely proportional to n^{-4}, rendering it exceptionally responsive to external electromagnetic fields. Simultaneously, the Rydberg energy level

spacing, inversely proportional to n^3, results in significantly smaller level spacing compared to ground state atoms, spanning the frequency range from MHz to THz [4], [5]. Leveraging these attributes, the Rydberg atom demonstrates high sensitivity, wide bandwidth, and traceability in precisely measuring microwave electric fields [6], [7]. Consequently, it finds diverse applications in electric field metrology [8], [9], [10], remote sensing [11], [12] and weak field measurement [13], [14].

The Rydberg atom has an abundance of energy levels, making it possible to measure the microwave electric field based on it almost continuously cover the frequency bands from microwaves to terahertz. Linear measurements, on the other hand, are typically limited to the MHz range around a single resonant transition. Most precision measurements of microwave electric fields utilizing the Rydberg atom are limited to a single frequency band. Achieving electric field measurements across a continuous frequency range needs real-time frequency hopping and switching among multiple Rydberg energy levels, imposing significant demands on the experimental system. This complexity hinders accurate measurement of the microwave electric field in a continuous broadband spectrum with Rydberg atoms. Additionally, factors such as the Rabi frequency of the coupling laser and the linewidths of any intermediate state influence the communication bandwidth of the Rydberg atom under a single resonance transition, placing constraints on channel capacity during communication. To address these challenges, the adoption of multi-channel solutions proves effective in expanding channel capacity, enabling more comprehensive wideband measurements.

In the communications field, the Rydberg atom replaces the traditional antenna with superior performance aspects that include sub-wavelength size, high dynamic range and self-calibration [15], [16], [17]. Moreover, receivers utilizing Rydberg atoms have proven successful in wireless communication through various modulation techniques, including amplitude modulation [18], [19], [20], [21], frequency modulation [22], [23], and phase modulation [24]. However, the time required for the establish of electromagnetically induced transparency in the interaction between light and atoms, coupled with the time needed to respond to sudden changes in the external electric field, imposes limitations on the utilization of Rydberg atom-based devices for communication, affecting the bandwidth of the sensor [25], [26]. Song Zhenfei et al. achieved communication and spectrum sensing with a wider bandwidth by employing continuously tunable RF carrier method. This offers a viable approach for multi-channel communication using the
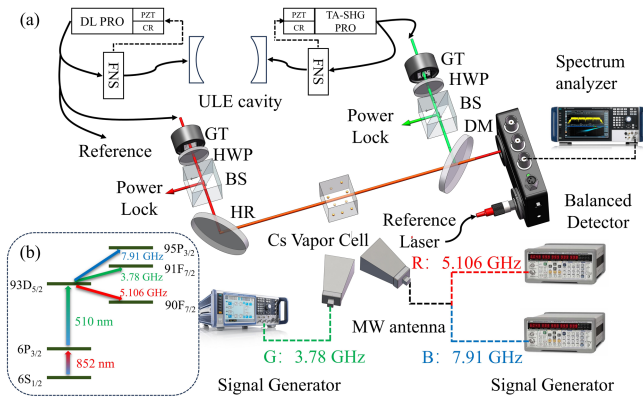
Fig. 1. (a) Experimental setup for image transmission based on the amplitude modulation technology of the Rydberg atomic antenna. FNS: Frequency noise servo system, ULE cavity: Ultra-low thermal expansion cavity, GT: Glan Taylor polarizer, HWP: half wave plate, BS: beam splitter (T: R=9:1), HR: high reflection dielectric mirror, DM: dichroic mirror. (b) Relevant energy levels of cesium Rydberg atoms. The probe laser at 852 nm and the coupling laser at 510 nm couple the transitions from ground state $6S_{1/2}$ to excited state $6P_{3/2}$ and excited state to Rydberg state $93D_{5/2}$, respectively. The $93D_{5/2}$ Rydberg state simultaneously interacts with the other three Rydberg states through three microwave fields.

same pair of Rydberg states [27]. In addition, studies have shown that different laser sizes and optical powers have an impact on bandwidth [28]. Subsequent studies have enhanced data transmission capabilities through the utilization of multi-band, multi-channel, and multiple atomic species [29], [30], [31], [32], thereby providing additional research references for channel expansion based on Rydberg atoms.

In this research, we implemented a microwave communication in a room-temperature cesium atom. Amplitude-shift keying modulation method was employed to achieve simultaneous multi-band reception in the C-band (7.91 GHz, 5.106 GHz) and S-band (3.78 GHz). Subsequently, we encoded RGB information from color image pixels to the independent frequencies of these three bands for transmission. Through the multi-channel frequency coding and simultaneous optimization of multi-channel signal amplitudes, we successfully achieved multi-channel radio communication reception at 3.78 GHz, 5.106 GHz, 7.91 GHz. This study shows high-fidelity digital color image transmission based on the frequency coding of the Rydberg atomic antenna, yielding a root mean square error of 4.806 and a mean square signal-to-noise ratio of 1.627 for image transmission fidelity. This study lays a significant research foundation to meet the requirements of high-speed broadband communication, Big Data transmission, and high-definition video streaming using Rydberg atoms.

II. EXPERIMENTAL SETUP

Fig. 1 depicts the experimental setup for image transmission based on Rydberg atomic antenna amplitude modulation method. The system comprises key components, including a laser system for exciting ground-state cesium atoms into the Rydberg excited state, a microwave field system supplying multi-band microwave carrier signals and amplitude modulation functions for image transmission, and a data acquisition

and analysis system facilitating collaborative measurement and analysis of spectral signals.

Fig. 1(b) illustrates a schematic diagram of the related energy levels of the cesium Rydberg atom. Utilizing a ladder-type two-photon process to excite cesium atoms to the Rydberg state, the coupling to different Rydberg states is then achieved through microwaves of different frequencies. The frequency of the probe laser, with a wavelength of 852 nm, was locked on the $6S_{1/2}, F = 4 \rightarrow 6P_{3/2}, F' = 5$ hyperfine transition. Simultaneously, the frequency of coupling laser, with a wavelength of 510 nm, was locked on $6P_{3/2}, F' = 5 \rightarrow 93D_{5/2}$ hyperfine transition. The experiment incorporated three microwave frequency bands: the resonance transition frequency of the Rydberg transition $93D_{5/2} \rightarrow 91F_{7/2}$ is 3.78 GHz, the resonance transition frequency of the Rydberg transition $93D_{5/2} \rightarrow 90F_{7/2}$ is 5.106 GHz, and the resonance transition frequency of the Rydberg transition $93D_{5/2} \rightarrow 95P_{3/2}$ is 7.91 GHz.

The experimental setup is depicted in Fig. 1(a). The laser system consists of two main laser sources. The probe laser (852 nm) is generated by a semiconductor laser (DL pro, Toptica), while the coupling laser (510 nm) is supplied by a tapered semiconductor laser amplifier (TA-SHG, Toptica). Both the 852 nm laser and the 1020 nm semiconductor seed laser are locked onto a 10 cm long ultra-low thermal expansion cavity (ULE). The frequency noise servo system (FNS) eliminates frequency noise from the probe and coupling lasers. Utilizing sideband locking technology, the FNS locks the probe laser and the coupling laser frequency to a high-precision optical resonator simultaneously. The phase modulator serves as the offset frequency device, enabling a linear frequency sweep within the 750 MHz range. The probe and coupling lasers are coupled from polarization-maintaining fiber to free space via a fiber collimator. A 3:1 fiber beam splitter precedes the feeding of the probe laser into the collimator. Here, three-quarters of the laser beam enters the collimator as the main beam, while a quarter is used as reference beam for the subsequent differential optical path. Subsequently, vertical polarization selection of the laser beam is achieved using a Glan-taylor prism and a half-wave plate, ensuring a polarization extinction ratio greater than 60 dB. After polarization purification, the probe and coupling lasers are separated by a beam splitter, with 10% of their power reserved for power monitoring and locking, effectively reducing intensity noise. The optical pathways of the probe laser and the coupling laser, transmitted in opposite directions, coincide in the cesium vapor, eliminating the Doppler background. The vapor dimensions are $20 \times 20 \times 20$ mm^3. Throughout the experiment, the beams used in the experiment are nearly parallel at the cell. The probe laser beam has Gaussian diameter of 1.9 mm, the coupling laser beam has Gaussian diameter of 2.0 mm. The coupling laser power is kept constant at 2 mW, the probe laser injected into the cell is about 22.5 μW. The Rabi frequency of the probe laser is maintained at $2\pi \times 3.620$ MHz, while that of the coupling laser is maintained at $2\pi \times 0.066$ MHz.

The microwave system provides three independent frequency microwave fields for image transmission and allows separate amplitude modulation of these fields. In this experiment, three microwave frequencies within the S-band and C-band

TABLE I
RELATIONSHIP BETWEEN PIXEL COLOR SCALE AND MODULATION FREQUENCY

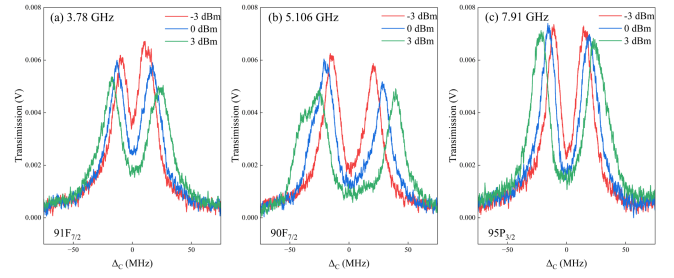| Color Scale	Modulation Frequency / kHz		
	Red	Green	Blue
0	20	40	60
1	20.05	40.05	60.05
...	...	...	...
254	32.70	52.70	72.70
255	32.75	52.75	72.75

Fig. 2. Transmission spectrum of probe laser passing through atoms with frequency detuning of coupling laser. The red line, blue line, and green line correspond to the results at microwave power of -3 dBm, 0 dBm, and 3 dBm, respectively. (a) The result for $93D_{5/2} \rightarrow 91F_{7/2}$ transition corresponds to a microwave frequency of 3.78 GHz. (b) The result for $93D_{5/2} \rightarrow 90F_{7/2}$ transition corresponds to a microwave frequency of 5.106 GHz. (c) The result of $93D_{5/2} \rightarrow 95P_{3/2}$ transition corresponds to a microwave frequency of 7.91 GHz.

were employed. The C-band frequencies (7.91 GHz, 5.106 GHz) were generated using two RF signal generators (SG386, Stanford Research Systems), while the S-band frequency (3.78 GHz) was generated by the signal generator (SMA100B, Rohde & Schwarz). The C-band microwaves were directed to free space via a standard gain horn antenna operating in the frequency range of 5.38 GHz–8.17 GHz and transmitted to a cesium atomic vapor. Similarly, the S-band microwaves were guided to free space by a standard gain horn antenna operating in the frequency range of 2.60 GHz–3.95 GHz and projected onto the cesium atomic vapor. Simultaneously, the internal modulation function of the RF source facilitated amplitude modulation for the three microwave fields, with a modulation depth of 20% and a modulation frequency ranging from 20 kHz to 60 kHz for sinusoidal signals.

The data acquisition and analysis system is mainly divided into three parts: electromagnetically induced transparency spectrum measurement analysis, frequency spectrum measurement analysis and image analysis. The probe laser after interacting with atoms is directed to one optical input port of the balanced photodetector (PDB210 A/M, Thorlabs), while the 852 nm reference laser is input to another optical port to counteract the DC shift of the photocurrent, thereby reducing photodetector saturation. Electromagnetically induced transparency spectra are obtained by scanning the coupling laser near the resonant frequency using a phase modulator. The spectral signal undergoes Fourier transformation and is recorded on a spectrometer (FSVA3044, Rohde & Schwarz). For color image transmission, each pixel is defined by three parameters: R, G, B (red, green, and blue), representing the three primary colors. The image utilizes an 8-bit color depth, meaning a digital image in R, G, and B spaces, where each color is represented by 256 levels. Theoretically, there are $256 \times 256 \times 256$ color combinations. To facilitate image transmission, a correspondence between modulation frequency and color scale is established. The modulation frequency band is divided into three sub-bands: $20 \sim 40$ kHz, $40 \sim 60$ kHz, and $60 \sim 80$ kHz, corresponding to the primary colors of red, green, and blue, respectively. The relationship between color scales and modulation frequencies is detailed in Table I. Each primary color order is subdivided into 256 degrees, and the channel spacing between adjacent frequency channels is set to 50 Hz. Subsequently, the intensity modulation of the three microwave fields is performed using three modulation signals of different frequencies, where each frequency corresponds to a degree of a primary color. The decoding modulation frequency aligns with the frequency scales for different primary colors

in the table, ultimately achieving the recovery and display of the image.

III. RESULTS AND DISCUSSION

In the four-level atomic system, a microwave field resonating with the two adjacent Rydberg state transitions alters the susceptibility of the probe laser. This change disrupts the coherence characteristics of the three-level system, causing reabsorption of the probe laser and generating the Autler-Townes splitting spectrum. Measurement of the transmission spectrum after the interaction of the probe laser with the atoms allows for the determination of the microwave electric field strength. The splitting of the probe laser transmission spectrum in relation to the intensity of the applied microwave field is detailed as follows [5]:

$$E = 2\pi \frac{\hbar}{\wp_{MW}} D \triangle f, \tag{1}$$

where $\hbar$ is the reduced Planck constant, $\wp_{MW}$ is the atomic dipole moment of the Rydberg level transition resonating with the microwave frequency, $\triangle f$ is the measured spectral splitting frequency spacing, and the D is the Doppler mismatch factor, and it depends on the frequency scanning laser during the spectral measurement. If the frequency of the probe laser is scanned, $D = \lambda_p/\lambda_c$, where λ_p and λ_c are the wavelengths of the probe and coupling laser, respectively. If the frequency of the coupling laser is scanned, $D = 1$.

Fig. 2 illustrates the transmission spectra of the probe laser passing through the atoms as a function of the coupling laser frequency detuning. The ordinate represents the transmitted intensity of the probe laser, and the abscissa is the frequency detuning of the coupling laser, with a frequency zero corresponding to the $6P_{3/2} - 93D_{5/2}$ Rydberg resonance transition. With the microwave field, the coherence characteristics of the three-level system are disrupted, leading to the Autler-Townes (AT) splitting. We measured the splitting spectra at different microwave powers (-3 dBm, 0 dBm, and 3 dBm) for various Rydberg transitions. As depicted in the figure, the splitting of the different Rydberg level transitions gradually increases with
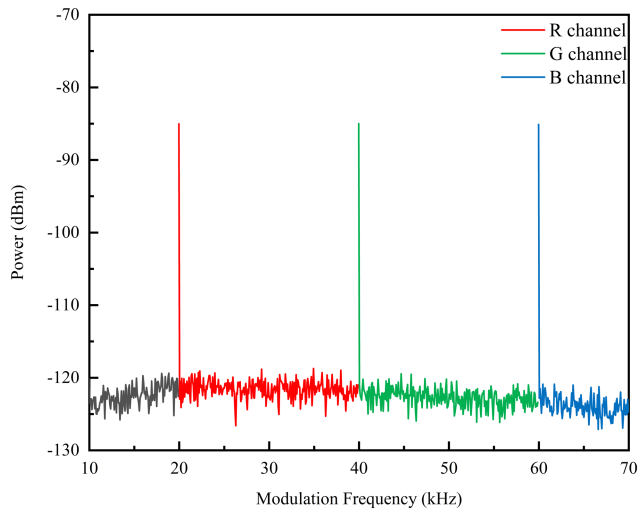
Fig. 3. Transmission spectrum of a pixel, the red line corresponds to the modulation frequency of the R channel, the green line corresponds to the modulation frequency of the G channel, and the blue line corresponds to the modulation frequency of the B channel.

Fig. 4. Flowchart of image transmission.

the increase in microwave power, consistent with the expectations from (1). However, at the same microwave power, the AT splitting interval and peak height of different Rydberg transitions exhibit distinct characteristics, attributed to the differing dipole moments of transitions between various Rydberg states. The rightmost AT peaks shift more than the leftmost AT peaks in Fig. 2(a) is mainly due to the energy level shift caused by the AC-Stark effect after the microwave power change, resulting in microwave frequency detuning. In Fig. 2(b), the double-peak feature on the leftmost AT peak in the green plot is due to the effect of magnetic sublevels. Through this analysis, we successfully discerned the characteristics of these three independent frequency transmission channels.

The independently adjustable three channels offer a platform for data transmission. We utilized this experimental system to validate high-fidelity image data transmission. Initially, the R, G, and B information of the image to be transmitted is retrieved, and the order of the primary color corresponds to the respective frequency is matched with previously described method. Subsequently, employing amplitude modulation within the RF signal source, the modulated signal is directed to free space through the horn antenna, transmitted to the cesium vapor, and interacts with the Rydberg atom. In the course of image transmission, the R, G, and B channels align with S-band (3.78 GHz), C-band (5.106 GHz), and C-band (7.91 GHz) microwaves, respectively. This implies that the microwave field of these three frequency bands acts on the Rydberg atom simultaneously, allowing the Rydberg atom to receive three frequency microwaves in the S-band and C-band within a single quantum state.

Fig. 3 illustrates the spectrum corresponding to the R, G, and B of a pixel in the transmitted image. To optimize the transmission process, we use the results obtained in Fig. 2 to adjust the microwave power of each channel, ensuring uniform modulated signal power results for the three parameters within a single pixel. In Fig. 3, the modulated signal power significantly exceeds
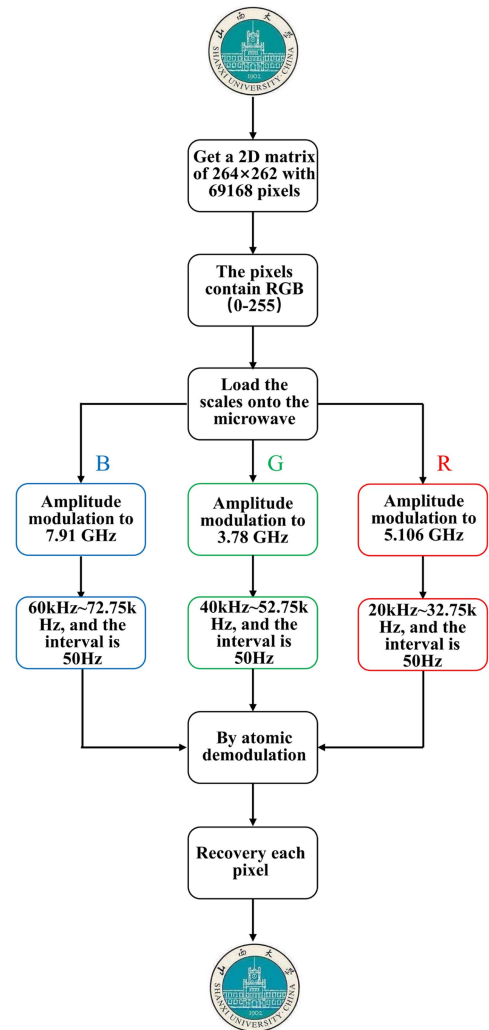
the noise level (at least 40 dB), fully meeting experimental requirements. On the modulation side, we employ signals at frequencies of 20 kHz, 40 kHz, and 60 kHz, respectively. The three distinctive modulation frequencies decoded from Fig. 3 also correspond to 20 kHz, 40 kHz, and 60 kHz. These frequencies are then mapped to the order represented in the respective channel. Analyzing the transmission result of a single pixel in Fig. 3, the characteristic spectral lines denote the 0 scale of red, the 0 of green, and the 0 of blue, respectively. Utilizing the information from this spectrum allows for the recovery of a single pixel in the image. After receiving information from all pixels, the entire image can be reconstructed. In this work, the frequency modulation range used for each channel is 12.75 kHz, with adjacent scales differing by 50 Hz. The smaller the frequency resolution and the smaller the frequency difference between adjacent scales, the greater the range that can be encoded within the achievable encoding bandwidth of the system. The image transmission process, depicted in Fig. 4, is principally divided into five components: decomposing the image to obtain the corresponding color scale for each pixel, mapping the modulation frequency to the primary color scale, modulating the microwave
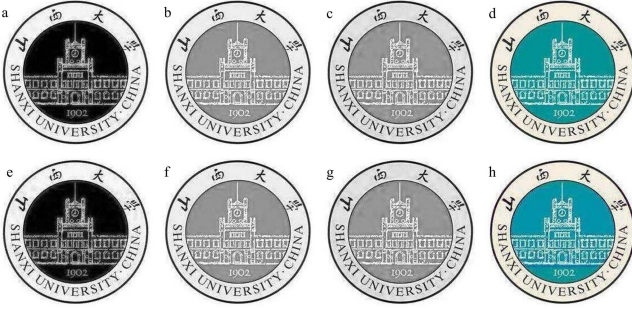
Fig. 5. Results before and after image transmission. (a)–(d) is the original image, a, b, and c are three R, G, and B monochromatic images decomposed from the original image d; (e)–(h) is the image recovered after transmission. e, f and g are three monochromatic images of R, G, and B received, while h is the color image recovered after transmission.

field by amplitude modulation, demodulating the color scale corresponding to the frequency, and ultimately recovering the final image. The whole process of image transmission is done pixel by pixel, the order of the R, G, and B channels obtained by each pixel decomposition is transmitted at the same time, as shown in Fig. 3, which represents the transmission result of one pixel.

Fig. 5 presents the results before and after the entire image transmission. Fig. 5(a)–(d) depict the original image, while Fig. 5(e)–(h) show the image recovered after transmission. Specifically, Fig. 5(a), (b), and (c) represent the three monochrome images of R, G, and B decomposed from the original Fig. 5(d). In parallel, Fig. 5(e), (f), and (g) portray the three monochrome images of R, G, and B after signal recovery, and Fig. 5(h) illustrates the color image recovered after transmission. In order to evaluate the quality and reliability of image transmission, we mainly analyze the fidelity of the image from the two perspectives: root mean square error and mean square signal-to-noise ratio. The formula for the root mean square error is expressed as follows:

$$e_{rms} = \sqrt{\frac{1}{MN} \sum_{x=0}^{M-1} \sum_{y=0}^{N-1} \left[\hat{f}(x,y) - f(x,y) \right]^2}, \quad (2)$$

The root-mean square signal-to-noise ratio is as follows:

$$SNR_{ms} = \frac{\sum_{x=0}^{M-1} \sum_{y=0}^{N-1} \left[\hat{f}(x,y) \right]^2}{\sum_{x=0}^{M-1} \sum_{y=0}^{N-1} \left[\hat{f}(x,y) - f(x,y) \right]^2}, \quad (3)$$

The input image, denoted as $f(x,y)$ consists of $M \times N$ pixels, where $x = 0, 1, 2, \ldots M-1$; $y = 0, 1, 2, \ldots N-1$ and the corresponding decoded image is $\hat{f}(x,y)$. Using (2) and (3) determined as the root mean square error of image transmission fidelity is 4.806, with a mean square signal-to-noise ratio of 1.627. Specifically, the root mean square error for the R, G, and B channels is 4.583, 0, 0, respectively, while the mean square signal-to-noise ratio is 1.543, infinity, infinity. At the same time, we used the peak signal-to-noise ratio and the structural similarity index to check the similarity of the input and the

transmitted images. The formula for the peak signal-to-noise ratio is expressed as follows:

$$PSNR = 10 \cdot \log_{10} \left(\frac{MAX^2}{MSE} \right) = 20 \cdot \log_{10} \left(\frac{MAX}{\sqrt{MSE}} \right), \quad (4)$$

Where MAX is the maximum pixel value in the image, MSE is a mean square error. Using (4), the peak signal-to-noise ratio of image transmission is determined as 29.998, with a structural similarity index of 0.9621. Specifically, peak signal-to-noise ratio for the R, G, and B channels is 30.768, infinity, infinity, respectively, while the structural similarity index is 0.9589, 1, 1. The value of the peak signal-to-noise ratio value represents the similarity of the image to the original image, the higher the value, the more similar the image is to the original image, and thus the better the image quality. Structural similarity index values range from 0 to 1, with larger images being more similar. If the two images are exactly the same, the structural similarity index value is 1. The result indicates that the G and B channels exhibit nearly error-free information transmission, whereas the R channel is influenced by additional frequency components, potentially leading to partial errors. This effect could be attributed to the presence of other frequency components in the R channel with modulation frequencies between 20 and 40 kHz. For the frequency coding method used in this paper, a single order of a single pixel corresponds to a modulation frequency. The signal demodulated by the atom at a single frequency has a sufficiently large signal-to-noise ratio, as shown in Fig. 3, to obtain an accurate modulation frequency and restore the corresponding order. The $40 \sim 60$ kHz range for the G channel and the $60 \sim 80$ kHz range for the B channel are not affected by other frequency components, so the image information can be completely restored.

The protocol demonstrates extensive applicability and facilitates the transmission of diverse files, including digital, image, sound, and video. Its flexibility is reflected in setting different frequency bands and determining the correspondence between the information to be transmitted and the modulation frequency, thereby achieving customized transmission of various types of information. Specifically, one only need to set different frequency bands, associate the information to be transmitted with the modulation frequency, then perform Fourier transform on the probe laser transmission spectrum signal, and finally decode the modulation frequency, then can successfully obtain the required information transmitted.

Fig. 6 presents the experimental results depicting the instantaneous bandwidths of atoms in various Rydberg states, reflects the relationship between the receiving capacity of the atomic antenna and the working frequency. The red dot shows the instantaneous bandwidth of microwave frequency of 5.106 GHz with the Rydberg state of $90F_{7/2}$; the green dot represents the instantaneous bandwidth of microwave frequency of 3.78 GHz with the Rydberg state of $91F_{7/2}$, while the blue dot illustrates the instantaneous bandwidth of microwave frequency of 7.91 GHz with the Rydberg state of $95P_{3/2}$. By modulating the amplitude of the microwave field at various frequencies, the corresponding
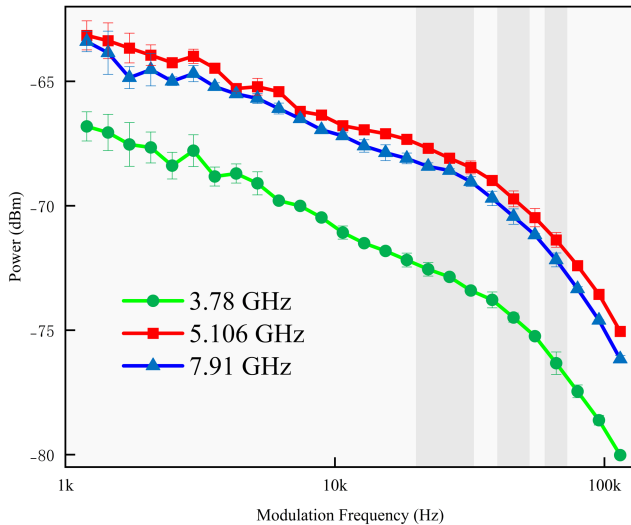
Fig. 6. Experimental results of the instantaneous bandwidth. The red, blue, and green lines represent the results at microwave frequencies of 5.106 GHz, 7.91 GHz, and 3.78 GHz, respectively. The illustration shows the modulation frequency range used in the experiment. The error bar is an average of 5 times.

signal magnitude is obtained. As the modulation frequency increases, the intensity signal gradually diminishes, influenced by the Rydberg state atomic lifetime, the Rabi frequency of the probe laser and the coupling laser. Each pixel transmitting a color image is characterized by three parameters: R, G, and B(corresponds to the three gray frequency ranges in the figure). The modulation band is divided into three subbands, aligning with the primary colors of red, green, and blue. The results in Fig. 3 indicate the system has a noise floor of -124 dBm and a signal-to-noise ratio of nearly 40 dB. The 20 ∼ 80 kHz range chosen in the experiment fully complies with the experimental conditions. The variance in signal power under a single channel stems from differences in the transition dipole moment between the Rydberg states.

IV. CONCLUSION

Utilizing room-temperature Rydberg atoms, we achieved the simultaneous reception of three microwave frequencies: C-band (7.91 GHz, 5.106 GHz) and S-band (3.78 GHz)–within a single quantum state. Employing these frequencies as carriers, we encoded the RGB information of frequency-coded color image pixels onto the respective carriers, and further facilitated multi-channel radio communication reception spanning from 3.7 GHz to 8 GHz. The high-fidelity digital color image transmission, based on the frequency coding of the Rydberg atomic antenna, resulted in a root mean square error of 4.806, a mean square signal-to-noise ratio of 1.627, a peak signal-to-noise ratio of 29.998 and a structural similarity index of 0.9589. Subsequently, we measured the maximum coding bandwidth of the atomic antenna system. Notably, this atomic-based receiver offers several advantages: 1) direct reading of the baseband signal by demodulating the atom, 2) enabling multi-channel reception, and 3) spanning a frequency range from MHz to THz.

REFERENCES

[1] T. F. Gallagher, "Rydberg atoms," *Rep. Prog. Phys.*, vol. 51, no. 2, pp. 143–188, 1988.
[2] M. Saffman, T. G. Walker, and K. Mølmer, "Quantum information with Rydberg atoms," *Rev. Modern Phys.*, vol. 82, no. 3, pp. 2313–2363, 2010.
[3] C. S. Adams, J. D. Pritchard, and J. P. Shaffer, "Rydberg atom quantum technologies," *J. Phys. B: At. Mol. Opt. Phys.*, vol. 53, no. 1, 2019, Art. no. 012002.
[4] H. Fan, S. Kumar, J. Sedlacek, H. Kübler, S. Karimkashi, and J. P. Shaffer, "Atom based RF electric field sensing," *J. Phys. B: At. Mol. Opt. Phys.*, vol. 48, no. 20, 2015, Art. no. 202001.
[5] J. A. Sedlacek, A. Schwettmann, H. Kübler, R. Löw, T. Pfau, and J. P. Shaffer, "Microwave electrometry with Rydberg atoms in a vapour cell using bright atomic resonances," *Nature Phys.*, vol. 8, no. 11, pp. 819–824, 2012.
[6] D. A. Anderson, R. E. Sapiro, and G. Raithel, "A self-calibrated SI-traceable Rydberg atom-based radio frequency electric field probe and measurement instrument," *IEEE Trans. Antennas Propag.*, vol. 69, no. 9, pp. 5931–5941, Sep. 2021.
[7] J. Yuan et al., "Quantum sensing of microwave electric fields based on Rydberg atoms," *Rep. Prog. Phys.*, vol. 86, no. 10, 2023, Art. no. 106001.
[8] C. L. Holloway et al., "Atom-based RF electric field metrology: From self-calibrated measurements to subwavelength and near-field imaging," *IEEE Trans. Electromagn. Compat.*, vol. 59, no. 2, pp. 717–728, Apr. 2017.
[9] M. T. Simons, A. B. Artusio-Glimpse, A. K. Robinson, N. Prajapati, and C. L. Holloway, "Rydberg atom-based sensors for radio-frequency electric field metrology, sensing, and communications," *Meas.: Sensors*, vol. 18, 2021, Art. no. 100273.
[10] Y. Shi et al., "Near-field antenna measurement based on Rydberg-atom probe," *Opt. Exp.*, vol. 31, no. 12, pp. 18931–18938, 2023.
[11] A. K. Robinson, N. Prajapati, D. Senic, M. T. Simons, and C. L. Holloway, "Determining the angle-of-arrival of a radio-frequency source with a Rydberg atom-based sensor," *Appl. Phys. Lett.*, vol. 118, no. 11, 2021, Art. no. 114001.
[12] J. Sedlacek, A. Schwettmann, H. Kübler, and J. Shaffer, "Atom-based vector microwave electrometry using rubidium Rydberg atoms in a vapor cell," *Phys. Rev. Lett.*, vol. 111, no. 6, 2013, Art. no. 063001.
[13] J. A. Gordon, M. T. Simons, A. H. Haddab, and C. L. Holloway, "Weak electric-field detection with sub-1 Hz resolution at radio frequencies using a Rydberg atom-based mixer," *AIP Adv.*, vol. 9, no. 4, 2019, Art. no. 045030.
[14] M. G. Bason et al., "Enhanced electric field sensitivity of RF-dressed Rydberg dark states," *New J. Phys.*, vol. 12, no. 6, 2010, Art. no. 065015.
[15] M. Jing et al., "Atomic superheterodyne receiver based on microwave-dressed Rydberg spectroscopy," *Nature Phys.*, vol. 16, no. 9, pp. 911–915, 2020.
[16] K. C. Cox, D. H. Meyer, F. K. Fatemi, and P. D. Kunz, "Quantum-limited atomic receiver in the electrically small regime," *Phys. Rev. Lett.*, vol. 121, no. 11, 2018, Art. no. 110502.
[17] H. Zou, Z. Song, H. Mu, Z. Feng, J. Qu, and Q. Wang, "Atomic receiver by utilizing multiple radio-frequency coupling at Rydberg states of rubidium," *Appl. Sci.*, vol. 10, no. 4, p. 1346, 2020.
[18] J. Yuan, T. Jin, L. Xiao, S. Jia, and L. Wang, "A Rydberg atom-based receiver with amplitude modulation technique for the fifth-generation millimeter-wave wireless communication," *IEEE Antennas Wireless Propag. Lett.*, vol. 22, no. 10, pp. 2580–2584, Oct. 2023.
[19] D. H. Meyer, K. C. Cox, F. K. Fatemi, and P. D. Kunz, "Digital communication with Rydberg atoms and amplitude-modulated microwave fields," *Appl. Phys. Lett.*, vol. 112, no. 21, 2018, Art. no. 211108.
[20] H. Li et al., "Rydberg atom-based AM receiver with a weak continuous frequency carrier," *Opt. Exp.*, vol. 30, no. 8, pp. 13522–13529, 2022.
[21] Y. Jiao, X. Han, J. Fan, G. Raithel, J. Zhao, and S. Jia, "Atom-based receiver for amplitude-modulated baseband signals in high-frequency radio communication," *Appl. Phys. Exp.*, vol. 12, no. 12, 2019, Art. no. 126002.
[22] D. A. Anderson, R. E. Sapiro, and G. Raithel, "An atomic receiver for AM and FM radio communication," *IEEE Trans. Antennas Propag.*, vol. 69, no. 5, pp. 2455–2462, May 2021.
[23] S. Kumar, H. Fan, H. Kübler, A. J. Jahangiri, and J. P. Shaffer, "Rydberg-atom based radio-frequency electrometry using frequency modulation spectroscopy in room temperature vapor cells," *Opt. Exp.*, vol. 25, no. 8, pp. 8625–8637, 2017.

[24] C. L. Holloway, M. T. Simons, J. A. Gordon, and D. Novotny, "Detecting and receiving phase-modulated signals with a Rydberg atom-based receiver," *IEEE Antennas Wireless Propag. Lett.*, vol. 18, no. 9, pp. 1853–1857, Sep. 2019.

[25] D. A. Anderson, R. E. Sapiro, and G. Raithel, "Rydberg atoms for radio-frequency communications and sensing: Atomic receivers for pulsed RF field and phase detection," *IEEE Aerosp. Electron. Syst. Mag.*, vol. 35, no. 4, pp. 48–56, Apr. 2020.

[26] R. Sapiro, G. Raithel, and D. Anderson, "Time dependence of Rydberg EIT in pulsed optical and RF fields," *J. Phys. B: At. Mol. Opt. Phys.*, vol. 53, no. 9, 2020, Art. no. 094003.

[27] Z. Song et al., "Rydberg-atom-based digital communication using a continuously tunable radio-frequency carrier," *Opt. Exp.*, vol. 27, no. 6, pp. 8848–8857, 2019.

[28] N. Prajapati et al., "TV and video game streaming with a quantum receiver: A study on a Rydberg atom-based receiver's bandwidth and reception clarity," *AVS Quantum Sci.*, vol. 4, no. 3, 2022, Art. no. 035001.

[29] C. Holloway et al., "A multiple-band Rydberg atom-based receiver: AM/FM stereo reception," *IEEE Antennas Propag. Mag.*, vol. 63, no. 3, pp. 63–76, Jun. 2021.

[30] Z.-K. Liu et al., "Deep learning enhanced Rydberg multifrequency microwave recognition," *Nature Commun.*, vol. 13, no. 1, 2022, Art. no. 1997.

[31] D. H. Meyer, J. C. Hill, P. D. Kunz, and K. C. Cox, "Simultaneous multiband demodulation using a Rydberg atomic sensor," *Phys. Rev. Appl.*, vol. 19, no. 1, 2023, Art. no. 014025.

[32] C. L. Holloway, M. T. Simons, A. H. Haddab, C. J. Williams, and M. W. Holloway, "A "real-time" guitar recording using Rydberg atoms and electromagnetically induced transparency: Quantum physics meets music," *AIP Adv.*, vol. 9, no. 6, 2019, Art. no. 065110.